RSC Advances

PAPER

View Article Online
View Journal | View Issue

Cite this: *RSC Adv.*, 2020, **10**, 35803

Electrical properties of $Ca_{12}Al_{14}O_{33}$ synthesised through polymer assisted deposition and glass crystallization routes

Yun Lv, Huaibo Yi, Tianjie Wei, Junwei Liu, Xiangyu Xu and Jungu Xu *

Received 17th August 2020
Accepted 21st September 2020

DOI: 10.1039/d0ra07082c

rsc.li/rsc-advances

In this paper, two new methods, polymer assisted deposition (PAD) and glass crystallization (GC) methods were reported for the first time to prepare oxide ion conductor $Ca_{12}Al_{14}O_{33}$, with their microstructures and electrical properties compared to that of a sample prepared by the traditional solid-state reaction (SSR) method. The results showed that these two new methods are effective for improving ceramic densities and oxide ion conductivities compared to the SSR method, and the ceramic prepared from the GC method in the present work possessed the highest level of ~94% of the theoretical density and ~1.0 × 10^{-3} S cm^{-1} at 900 °C for the bulk conductivity. A new bond valence method was applied to study the oxide ion conducting mechanism, which revealed an exchange process between the free oxide ion and the framework ion, and the wide windows connecting the Ca–Al–O framework cages were shown to be the key factor limiting oxide ion transport.

Introduction

Oxide ion conductors are attracting increasing attention due to their application as electrolytes in solid-oxide fuel cells (SOFCs).[1–4] The state-of-the-art electrolyte used for commercially available SOFCs is yttria-stabilized zirconia (YSZ). However, this material can only meet the oxide ion conductivity demand at a working temperature higher than 800 °C.[5–7] Such a high temperature imposes a technical challenge for electrode material selection and their long-term stability, which therefore limits the widespread application of SOFCs and stimulates the discovery of new oxide ion conductors with high conductivities at intermediate temperature (400–700 °C). To date, some new structural families, such as apatites,[8,9] scheelites,[10,11] mayenites,[12,13] melilites,[14–17] and so on, have been identified to possess pure oxide ion conductivities and have good application potential in SOFCs. Among these new structural families, the mayenite $Ca_{12}Al_{14}O_{33}$ is also well-known for its optical properties,[18] electronic conducting properties when being converted into electride,[19] and the more recently reported thermal energy storage properties.[20] For the oxide ion conducting properties, these were first reported by M. Lacerda *et al.* with a modest level, inferior to that of YSZ at a given temperature.[21–23] Nevertheless, its relatively low cost of raw materials makes it still competitive if the oxide ion conductivity could be improved. To this end, several works using a cation doping strategy have been carried out, such as zinc single doping or zinc and phosphorus co-doping,[24,25] iron-doping,[26] cobalt-doping,[27] gallium-doping,[28] and vanadium-doping[29] on Al atom sites. For the zinc-, phosphorus-, or iron-doped materials, an even lower conductivity was observed when compared to that of parent $Ca_{12}Al_{14}O_{33}$. While for the cobalt, gallium, and vanadium doped samples, although the conductivities could be slightly improved, the low solid solution hindered their further conductivity enhancements. Other elements, including copper,[30,31] nickel,[32] manganese,[33] iridium,[34] bismuth,[35] and Ln^{3+}[Tb/Sm/Er/Nd/Yb/Ho/Pr][36] were also reported to be incorporated into the mayenite structure, but without oxide ion conductivity being investigated.

All these doped samples with low solid solution limits as stated above are mainly synthesized by traditional solid-state reaction method or through growing single crystals using the floating zone technique[37] or Czochralski method.[38] To investigate the effect of preparation condition on sinterability and electrical property, M. Matsuda *et al.* prepared the parent $Ca_{12}Al_{14}O_{33}$ material by mixing the raw materials through a solution method.[21] The sinterability and electrical property were then compared to the sample synthesized by the traditional solid-state reaction method in which the raw materials were mechanically mixed. The results showed a great enhancement in conductivity for the solution method prepared sample due to the better sinterability and densification. As in a similar hydrothermal synthesis, S. Fujita *et al.*[39] prepared Si-substituted mayenite $Ca_{12}Al_{14-x}Si_xO_{33+0.5x}$ with the high solid solution of $0 \leq x \leq 4$. Although these Si-substituted materials are stable only below 600 °C and

MOE Key Laboratory of New Processing Technology for Nonferrous Metal and Materials, Guangxi Universities Key Laboratory of Non-ferrous Metal Oxide Electronic Functional Materials and Devices, College of Materials Science and Engineering, Guilin University of Technology, Guilin 541004, P. R. China. E-mail: xujungu@glut.edu.cn

without oxide ion conductivities being reported, it gave us a hint that the low doping level as reported in previous works may be remarkably improved by a new synthesis method. Thus, developing new methods to prepare the mayenite-based materials may be an important way to optimize their sinterability, extend the solid solution limit, and finally improve their oxide ion conductivities. In addition, as debates existing in the oxide ion conduction mechanism in $Ca_{12}Al_{14}O_{33}$,[12,13,22] it is essential to make it clear to indicate a direction for its performance optimization.

In this paper, two new methods, polymer assisted deposition (PAD) method and glass crystallization (GC) method, are applied to prepare $Ca_{12}Al_{14}O_{33}$ material for the first time, with their electrical properties and microstructures being studied in detail and compared with that yielded from solid-state reaction method. Moreover, the oxide ion diffusion path in $Ca_{12}Al_{14}O_{33}$ was investigated by a new approach, the bond valence (BV) method, for the first time. This method had been proved to be reliable and successful in simulating the conduction mechanism for ionic conductors.[40,41]

Methods

Synthesis

(1) For samples prepared by polymer assisted deposition (PAD) method, $Ca(NO_3)_2 \cdot 4H_2O$ (Alfa Aesar, >99% purity) and $Al(NO_3)_3 \cdot 9H_2O$ (Alfa Aesar, >99.99% purity) were used as metal precursors and soluble polyethyleneimine (PEI) (Alfa Aesar, >99% purity) as the complexing agent. The Ca and Al precursor were first separately deposited in PEI in deionized water solution, and these two solutions were then mixed together, followed by a heating treat to evaporate water until finally burning out the PEI, yielding amorphous $Ca_{12}Al_{14}O_{33}$ precursor which was then fired at 1000 °C to obtain crystallized powder $Ca_{12}Al_{14}O_{33}$ product. To prepare ceramic samples for electrical property measurements, the powders were pressed into pellets and then calcined at 1300 °C for 12 h. (2) For the glass crystallization (GC) method, the well-mixed and grounded raw materials were first pressed into pellets with a diameter of 4 mm, which was then placed in an aerodynamic levitator coupled to a CO_2 laser heating system to achieve vitrification. The pellets were thus heated up to about 1850 °C for a few seconds to homogenize and subsequently quenched down to room temperature at a rate of roughly 300 °C s^{-1} by simply turning off the lasers, yielding glass beads. The crystallization process was then studied by heat treatment performed in the open air at 920 °C or higher temperature. (3) For comparison, $Ca_{12}Al_{14}O_{33}$ samples were also prepared by a solid-state reaction (SSR) method, using $CaCO_3$ (Alfa Aesar, >99% purity), Al_2O_3 (Alfa Aesar, >99% purity) as starting raw materials. The stoichiometric weighted, evenly mixed, and well-ground raw materials were first fired at 1000 °C for 12 hours to drive off CO_2. After regrinding, the pre calcined powders were uniaxially pressed into pellets and sintered at 1300 °C for 12 hours. Archimedes principle was applied to estimate the densities for all these prepared ceramics.

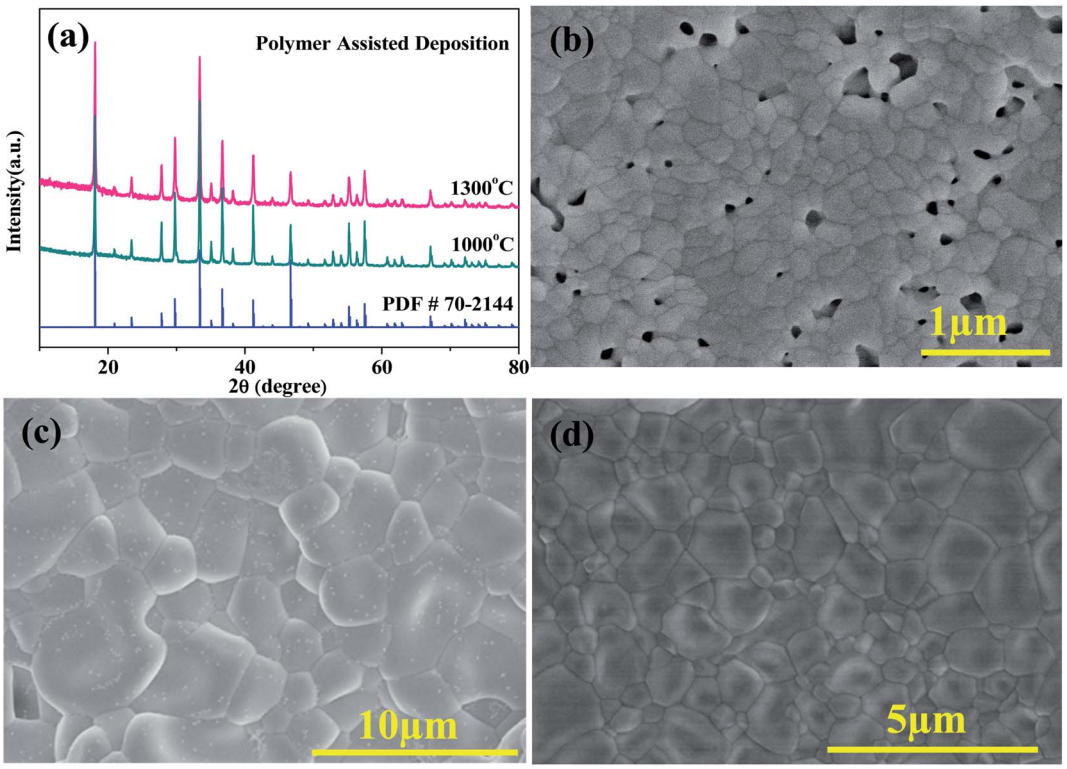

Fig. 1 (a) XRD patterns of the $Ca_{12}Al_{14}O_{33}$ samples from PAD method calcined at 1000 °C and 1300 °C, (b) and (c) show the microstructures of samples firing at 1000 °C and 1300 °C, respectively; (d) presents the particle size of the ceramic sample prepared by SSR method at 1300 °C.

Characterization

The XRD characterizations were performed on a Panalytical X'pert Pro X-ray diffractometer with Cu Kα radiation. *In situ* variable temperature, XRD (VTXRD) measurements were carried out using a HTK1200N Anton Paar oven chamber. The morphology was investigated using scanning electron microscopy (SEM) (S-4800, Hitachi, Japan). HRTEM imaging and EDS analysis were performed on a JEM-2100F (Japan) transmission electron microscopy. Electrochemical impedance spectroscopy (EIS) measurements were performed with a Bio-Logic VSP instrument over a 10^6 to 10^{-1} Hz frequency range. Before the EIS measurements, electrodes were formed by coating platinum paste on opposite faces of the pellets and fired at 750 °C for 3 hours to remove any organic components. Before the impedance measurements, the temperature was equilibrated at each setpoint for 30 minutes. Differential Scanning Calorimetry (DSC) was performed on the STA8000 thermal analysis instrument in airflow. The crystallization temperatures of glass were determined from 25 mg powder samples, with a heating rate of 10 °C min^{-1}.

Bond valence-based energy landscapes (BVELs) for a test ion O^{2-} in the $Ca_{12}Al_{14}O_{33}$ crystal structure (ICSD #6287) were calculated using the program 3DBVSMAPPER.[42] The spatial resolution was set to 0.2 Å.

Results and discussions

Phases and microstructures

As for the PAD method, fully crystallized and pure phase $Ca_{12}Al_{14}O_{33}$ material can be obtained by calcining the amorphous precursor at 1000 °C, as checked by the XRD pattern shown in Fig. 1a. However, the density of a pellet fired at this temperature is only ~69% of the theoretical density. The particle sizes observed in SEM analysis (Fig. 1b) on such a pellet are typically around 100–200 nm, and the pores demonstrated in the picture can be ascribed to the combustion of incompletely burned polymer in the precursor. Thus, to get a dense ceramic for electrical property measurement, the powders calcined at 1000 °C were then reground, pressed into pellets, and fired at 1300 °C. The phase purity and microstructure are displayed in Fig. 1a and c, respectively. It is seen that a pure phase with an average particle size of ~3.0 μm can be gained. The particle sizes are thus apparently increased and even larger than that prepared by the SSR method (0.25–1.5 μm and average in ~1.0 μm as shown in Fig. 1d) at the same firing temperature. The ceramic density was also improved to ~92% of the theoretical density, higher than the ceramic from the SSR method in this work (~90%).

For the glass crystallization method, the as-made colorless and transparent glass beads achieve a maximum size of ~3.0 mm in diameter. These glass beads were first ground into powders for DSC measurement, which reveals a single crystallization peak at ~920 °C, as presented in Fig. 2a. The presence of a single peak and no further exothermic peak at higher temperatures seem to indicate a congruent crystallization process which is required to eventually elaborate a dense and single-phase ceramic.[43] To confirm this congruent crystallization process, *in situ* variable temperature powder XRD measurements were then carried out from room temperature to 1000 °C (Fig. 2b). It reveals that only the mayenite phase crystallizes from 900 °C and no other crystalline phase was formed over the whole measured temperature range. The minor deviation in crystallization temperatures derived from DSC and VTXRD results can be ascribed to the different temperature detection precisions for the furnaces used for DSC and VT-XRD. Thermal treatment at temperature 900 °C in a furnace under the air atmosphere was then performed on glass beads in order to synthesize a fully crystallized mayenite material, *i.e.* a ceramic, in a single step, for subsequent electrical property measurements. However, heat treat at this temperature did not result in crystallized samples, regardless of heat treatment time, suggesting the thermodynamically inaccessible nature at this temperature. Thus, the annealing was then performed at a higher temperature of 920 °C. For 2 hours, the products show a partial crystallization behavior, as indicated by a broad rise in background centered at ~22° 2θ in the XRD pattern, and the obtained beads are also transparent, as the inset shows in Fig. 2c. This partial crystallization behavior was also further verified by HRTEM (Fig. 2d), from which we can see that besides the nano-crystalline region, the remaining part in the picture can be ascribed to amorphous $Ca_{12}Al_{14}O_{33}$. The element distribution analysis (Fig. 2e) revealed high homogeneity of the product and no segregation was observed. Prolong the annealing time to 5 hours would, however, lead to cracks of these beads into many little pieces (<1 mm in diameter) with irregular shapes. Although these little pieces have better crystallinity that can be checked by subsequent XRD measurement, such a small size makes it almost impossible to carry out electrical study experiments on an individual piece. Thermal treats at 950 °C or even higher temperatures for 2 hours or longer were also tried, but all failed and resulted in well-crystallized but cracked little pieces. The crack in these beads mainly arises from the huge internal thermal stress introduced in the glass beads preparing stage by extremely heating and cooling rates. Optimized annealing processes, *e.g.* using a much slower heating and cooling rates (1 °C min^{-1}), did not work either. Therefore, to obtain a well-crystallized ceramic pellet for electrical property studies, the partially or completely crystallized samples that precalcined at 920 °C or 950 °C has to be ground into powders and then pressed into pellets, followed by firing at 1300 °C that is the same as used in the SSR and PAD method in this work. The phase and microstructure of the final product obtained at 1300 °C were demonstrated in Fig. 2c and f, respectively. We can see that the product is phase pure and particle sizes are around 10–20 μm, with a ceramic density of ~95% of its theoretical value, close to the density of a ceramic that prepared by sintering at a higher temperature of 1350 °C as described in previous works.[21,44] The particle size and ceramic density thus pronounced larger than that for the SSR and PAD methods. The particle sizes and densities of ceramics prepared by these three different methods but with the same final firing temperature of 1300 °C are summarized in Table 1.

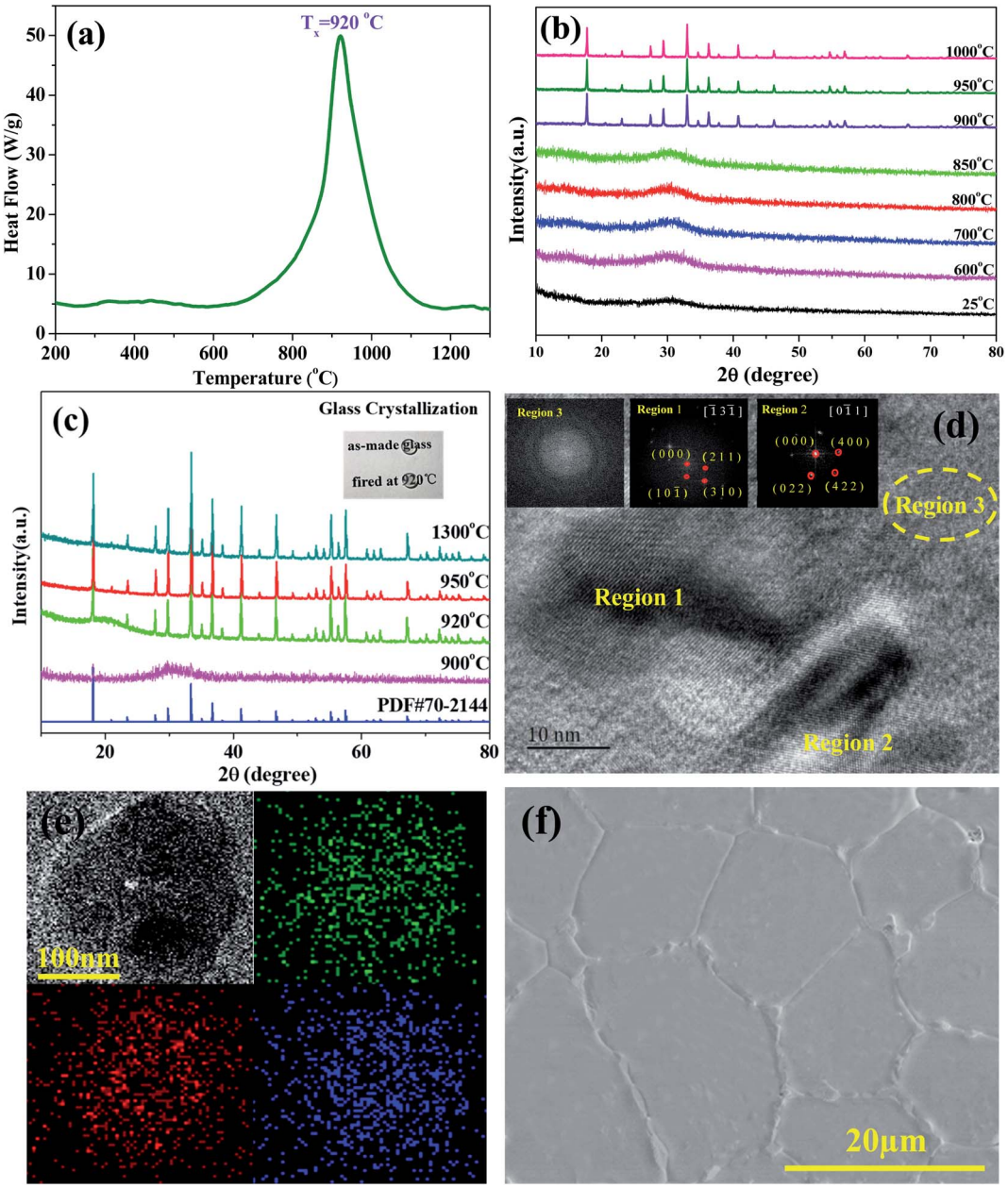

Fig. 2 (a) and (b) show the DSC curve and VTXRD patterns for as-made $Ca_{12}Al_{14}O_{33}$ glass, respectively; (c) shows the XRD patterns of the products of the as-made glass beads fired at different temperatures; (d) HRTEM micrographs and FFT graphs of $Ca_{12}Al_{14}O_{33}$ prepared by GC method at 920 °C; (e) is the EDS elemental distribution maps for the partially crystallized products at 920 °C in GC method; (f) show the microstructures of samples calcined at 1300 °C in GC method.

Table 1 Density and particle size of $Ca_{12}Al_{14}O_{33}$ ceramics prepared by three different methods but the same final firing temperature of 1300 °C

Method	Ceramic density	Particle size
SSR	90% of theory	0.25–1.5 μm, average in ~1.0 μm
PAD	92% of theory	2.0–5.0 μm, average in 3.0 μm
GC	94% of theory	10.0–20.0 μm, average in ~15.0 μm

Electrical properties

The oxide ion conductions of $Ca_{12}Al_{14}O_{33}$ materials prepared by SSR, PAD, and GC methods as stated above were studied by AC impedance spectroscopy, and the Arrhenius plots for bulk conductivities in these samples are shown in Fig. 3a. It can be seen that for the ceramics prepared at the same final firing temperature 1300 °C, the sample prepared from the glass crystallization method has the highest bulk conductivity, and about one order of magnitude higher than that of the sample from the SSR method which shows the lowest conductivity among these three samples. A medium conductivity was

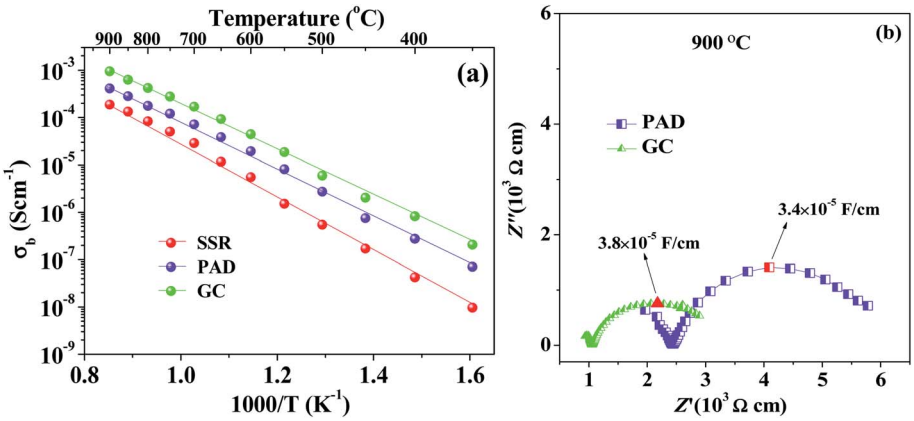

Fig. 3 (a) Arrhenius plots of bulk conductivities for $Ca_{12}Al_{14}O_{33}$ prepared by SSR, PAD, and glass crystallization methods at 1300 °C. (b) Complex impedance plots recorded at 900 °C of $Ca_{12}Al_{14}O_{33}$ synthesized by PAD (purple) and GC (green) method.

revealed for the sample synthesized by the PAD method. The conductivities in these samples can be well related to their particle sizes and ceramic densities. The larger particle size and higher ceramic density with reduced grain boundary lead to higher conductivity, as the bulk conductivity of a ceramic is deduced from the total impedance of grain and grain boundary, thus the higher density with less grain boundary would reduce the total resistance and result in higher conductivity. In fact, as had been reported by Irvine and West *et al.*, the controlled sintering is imperative to lower the grain boundary impedance,[44] and the optimum sintering temperature is around 1350 °C, close to the melting pointing. In the present work, we just fixed the final sintering temperature at 1300 °C and to investigate the effects of sample preparation methods on the conductivity. The conductivity for the sample prepared from the GC method here is comparable with that reported in Matsuda's work[21] where the sample was finally fired at 1350 °C. The nature of oxide ion conduction in these samples can be confirmed by the collapse of electrode response in a complex plot at elevated temperature. Fig. 3b shows typical complex plots recorded at 900 °C for samples prepared by both PAD and GC methods. We can see that the arcs at low frequency for these two samples show capacitances of $\sim 10^{-5}$ F cm^{-1}, which can be no doubt ascribed to electrode responses, corresponding to the enhanced kinetics of the oxygen ion diffusion and charge transfer reaction of $O_2 + 2e \leftrightarrow 2O^{2-}$ along with the sample–electrode interface.[43] Therefore, here we can make a conclusion that the PAD and GC methods can effectively improve the ceramic sinterability and hence resulted in higher oxide ion conduction. These two methods may also have great potential in preparing doped $Ca_{12}Al_{14}O_{33}$ materials with a high substitution degree.

Oxide ion migration paths

The oxide ion conduction in $Ca_{12}Al_{14}O_{33}$ is relative to its particular crystal structure, a cubic nanoporous zeolite-like structure (a = 11.98 Å, space group $I\bar{4}3d$, $Z = 2$). There are 64 out of 66 oxide ions fixed in the Ca–Al–O framework composed of 12 cages per unit cell. Each cage has a width of ~6 Å and is surrounded by 8 other cages with ~3.7 Å wide windows. The remaining two oxygen ions randomly occupy the centers of two of these cages, and thus loosely coordinated by cations and termed as 'free' oxygen. Therefore, the unit cell can be expressed by the chemical

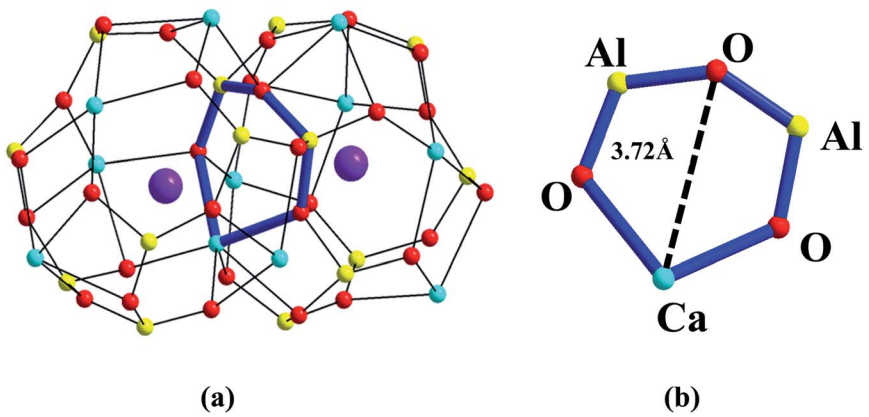

Fig. 4 Scheme of (a) two connecting cages, and (b) the window between two cages in $Ca_{12}Al_{14}O_{33}$. The blue, yellow, red, and purple spheres represent Ca, Al, framework O, and free O atoms, respectively.

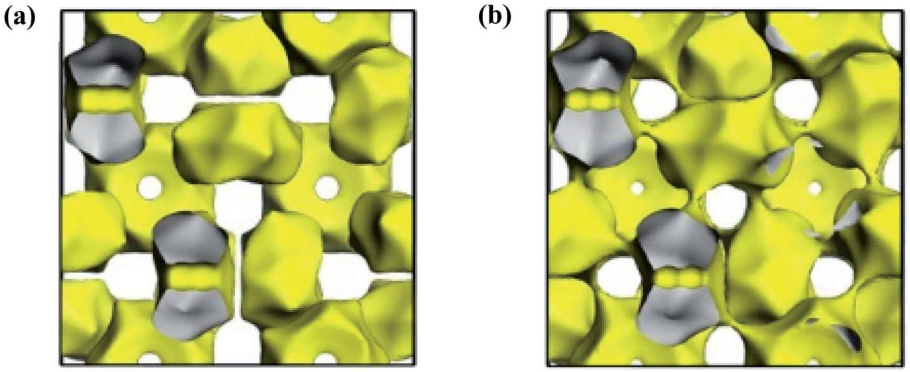

Fig. 5 The bond valance energy landscape at a low (a) and high (b) isosurface energy value.

formula $[Ca_{24}Al_{28}O_{64}]^{4+}\cdot 2O^{2-}$, and the schematic crystal structure is demonstrated in Fig. 4. The high mobility of free oxygen ions is an important factor for $Ca_{12}Al_{14}O_{33}$ to become an oxide-ion conductor, and these free oxide ions are initially thought to transport directly through the wide windows to a neighboring cage,[12] *i.e.* interstitial diffusion mechanism. This mechanism was then questioned by molecular dynamics and *ab initio* calculations by Sushko *et al.*,[22] which suggested that the diffusion processes are dominated by the exchange of free oxide ions with the framework. In this exchange mechanism, the migrating free oxygen ion will kick-out and replace one framework oxygen ion, which then goes into the next cage. This exchange mechanism was then further supported by high-temperature neutron powder diffraction,[13,23] and oxygen isotope exchange experiments.[45,46]

In this work, we investigated the possible oxide ion migration paths by the bond valence method for the first time. This method has been discussed in a range of earlier studies about how it be used to analyze ion transport pathways statistically from crystal structure data.[41,47–50] In a nutshell, it is based on the bond-valence sum (BVS) rule from Pauling's electrostatic valence concept.[51] It postulates that the BVS of an atom in a crystal structure almost equals the absolute value of its oxidation state, which can be expressed as the following relation:

$$V_i = \sum S_{ij} \quad (1)$$

where V_i is valence, *i.e.* formal oxidation state, S_{ij} is the bond valence for the pair of ions i and j, and can be described as the following exponential function

$$S_{ij} = \exp\frac{R - R_{ij}}{B} \quad (2)$$

where R and B are constant parameters,[52,53] R_{ij} is the distance between ions i and j. The bond valence sums (BVS) can thus be calculated not only for a crystallographic site actually occupied by atoms but for any arbitrary position in the unit cell. For a probe ion in a given position, the closer the calculated BVS to its oxidation state the more likely this position to be an intermediate transition point for the migration of this ion between equilibrium sites. For a bond valence method calculation, the test ion was placed sequentially at all points of a three-dimensional grid covering a unit cell. Positions with a low bond-valence mismatch ($V_i - \sum S_{ij}$), and hence indicating low site energy, connecting equilibrium sites forms an infinite network and suggests a potential migrating pathway.[52] Herein, the bond valence energy landscapes (BVEL) of O^{2-} ions in the unit cell of mayenite $Ca_{12}Al_{14}O_{33}$ was calculated using a spatial resolution of 0.2 A. Fig. 5 shows the calculation results. One can see that with a relatively low isosurface energy value, as displayed in Fig. 5a with yellow area, the oxide ion's migration is mainly limited in isolated cages, demonstrating a clear exchange between the free oxide and framework oxygen. As the isosurface energy value increasing, paths between two neighboring cages *via* the centers of the connecting windows gradually emerged. As can be appreciated from Fig. 5b, each isolated isosurface cage connected through bottlenecks to eight neighboring cages, thus forming a 3D infinite oxide ion migration network. These bottlenecks go through exactly the centers of wide windows between cages. Therefore, the oxide ion in $Ca_{12}Al_{14}O_{33}$ is most likely to transport by an exchange mechanism as reported in previous work. Moreover, transporting the oxide ion through the centers of wide windows seems to be inevitable, and passing through these windows is a rate-limiting step for the 3D oxide ion migration in $Ca_{12}Al_{14}O_{33}$. In addition, the results did not provide evidence for a pathway from free oxide ions directly to the center of wide windows, which therefore excluding the possibility of interstitial diffusion mechanism.

Conclusion

In this paper, the oxide ion conductor $Ca_{12}Al_{14}O_{33}$ was prepared by two new ways, PAD and GC methods, along with microstructures and electrical properties reported. The results show that the new methods can effectively increase the particle sizes and densities of $Ca_{12}Al_{14}O_{33}$ ceramic, and the product obtained from the GC method has the highest level, which therefore resulted in the highest conductivities among the ceramics prepared using the methods reported in the present work, $\sim 1.0 \times 10^{-3}$ S cm^{-1} at 900 °C for the bulk conductivity. A new bond valence method was applied for the first time to investigate the oxide ion transporting mechanism in $Ca_{12}Al_{14}O_{33}$. The results strongly suggest an

exchange mechanism involving the free oxide ions and framework ion, and passing through the centers of the wide windows between Ca–Al–O cages is inevitable and a rate-limiting step for the 3D oxide ion migration.

Conflicts of interest

There are no conflicts of interest to declare.

Acknowledgements

Guangxi Natural Science Foundation (2017GXNSFAA198203), National Natural Science Foundation of China (No. 21965008), "High-level innovation team and outstanding scholar program of Guangxi Institutes" are acknowledged for financial support.

References

1 L. Yu, M. Tade and Z. Shao, *Solid Oxide Fuel Cells: From Materials to System Modeling*, 2013, vol. 123, pp. 26–55.
2 A. Subardi, K. Y. Liao and Y. P. Fu, *RSC Adv.*, 2017, **7**, 14487–14495.
3 D. Jeong and G. Kim, *Ceramist*, 2018, 21.
4 Y. Lyu, J. Xie, D. Wang and J. Wang, *J. Mater. Sci.*, 2020, **55**, 7184–7207.
5 Z. L. M. Botello, A. Montenegro, N. G. Osorio, M. Huvé, C. Pirovano, D. R. Småbråten, S. M. Selbach, A. Caneiro, P. Roussel and G. H. Gauthier, *J. Mater. Chem. A*, 2019, **7**, 18589–18602.
6 S. Ryu, W. Yu, I. Chang, T. Park and S. W. Cha, *Ceram. Int.*, 2020, **46**, 12648–12655.
7 N. Chuankrerkkul, S. Chauoon, M. Meepho and R. Pornprasertsuk, *Key Eng. Mater.*, 2017, **751**, 467–470.
8 Y. Tianrang, Z. Hailei, F. Mengya, W. Konrad, W. Jie and D. Zhihong, *J. Eur. Ceram. Soc.*, 2019, 424–431.
9 D. Marrero-Lopez, P. Diaz-Carrasco, J. Pena-Martinez, J. C. Ruiz-Morales and J. R. Ramos-Barrado, *Fuel Cells*, 2011, **11**, 65–74.
10 X. Yang, A. J. Fernandezcarrion, J. Wang, F. Porcher, F. Fayon, M. Allix and X. Kuang, *Nat. Commun.*, 2018, **9**, 4484.
11 R. J. Packer, S. J. Skinner, A. A. Yaremchenko, E. V. Tsipis, V. V. Kharton, M. V. Patrakeev and Y. A. Bakhteeva, *J. Mater. Chem.*, 2006, **16**, 3503–3511.
12 J. T. S. Irvine and M. Lacerda, *Nature*, 1988, **23**, 1033–1038.
13 H. Boysen, M. Lerch, A. Stys and A. Senyshyn, *Acta Crystallogr.*, 2007, **63**, 675–682.
14 J. Xu, J. Wang, X. Tang, X. Kuang and M. Rosseinsky, *Inorg. Chem.*, 2017, **56**, 6897–6905.
15 X. Kuang, M. A. Green, H. Niu, P. Zajdel, C. Dickinson, J. B. Claridge, L. Jantsky and M. J. Rosseinsky, *Nat. Mater.*, 2008, **7**, 498–504.
16 J. Xu, X. Kuang, E. Veron, M. Allix, M. R. Suchomel, F. Porcher, C. Liang, F. Pan and M. Wu, *Inorg. Chem.*, 2014, **53**, 11589–11597.
17 J. Xu, J. Wang, A. Rakhmatullin, S. Ory, A. J. Fernández-Carrión, H. Yi, X. Kuang and M. Allix, *ACS Appl. Energy Mater.*, 2019, **16**, 3503–3511.
18 M. M. Rashad, A. G. Mostafa and D. A. Rayan, *J. Mater. Sci.: Mater. Electron.*, 2015, **27**, 1–10.
19 S. Matsuishi, Y. Toda, M. Miyakawa, K. Hayashi, T. Kamiya, M. Hirano, I. Tanaka and H. Hosono, *Science*, 2003, **301**, 626–629.
20 A. Zaki, A. Gutierrez, M. Schmidt, D. Bielsa, M. Linder and A. Faik, *J. Energy Storage*, 2020, **31**, 101647.
21 M. Matsuda, Y. Inda, W. Hisamatsu, K. Yamashita and T. Umegaki, *J. Mater. Sci. Lett.*, 1996, **15**, 933–934.
22 P. V. Sushko, A. L. Shluger, K. Hayashi, M. Hirano and H. Hosono, *Phys. Rev. B: Condens. Matter Mater. Phys.*, 2006, **73**, 014101.
23 H. Jian, L. Valenzano and G. Sant, *Chem. Mater.*, 2015, **27**, 4731–4741.
24 J. T. S. Irvine and A. R. West, *Solid State Ionics*, 1990, **40**, 896–899.
25 K. Khan, A. K. Tareen, M. Aslam, K. H. Thebo, U. Khan, R. Wang, S. S. Shams, Z. Han and Z. Ouyang, *Prog. Solid State Chem.*, 2019, **54**, 1–19.
26 S. G. Ebbinghaus, H. Krause, D. Lee and J. Janek, *Cryst. Growth Des.*, 2014, **14**, 2240–2245.
27 H. Yi, Y. Lv, V. Mattick and J. Xu, *Ionics*, 2019, **25**, 5105–5115.
28 H. Yi, Y. Lv, Y. Wang, X. Fang, V. Mattickb and J. Xu, *RSC Adv.*, 2019, **9**, 3809–3815.
29 A. S. Tolkacheva, S. N. Shkerin, S. V. Plaksin, A. A. Pankratov, N. I. Moskalenko and I. Ceramics, *Refract. Ind. Ceram.*, 2019, **60**, 109–114.
30 S. Maurelli, M. Ruszak, S. Witkowski, P. Pietrzyk, M. Chiesa and Z. Sojka, *Phys. Chem. Chem. Phys.*, 2010, **12**, 10933–10941.
31 J. R. Salasin, S. E. A. Schwerzler, M. R. Koehler, D. J. Keffer and C. Rawn, *Materialia*, 2018, **4**, 466–477.
32 M. Teusner, R. A. De Souza, H. Krause, S. G. Ebbinghaus and M. Martin, *Solid State Ionics*, 2016, **284**, 25–27.
33 L. Palacios, S. Bruque and M. A. G. Aranda, *Phys. Status Solidi*, 2008, **245**, 666–672.
34 R. Stoser, M. Nofz, W. Gesner, C. Schroter and G. Kranz, *J. Solid State Chem.*, 1989, **81**, 152–164.
35 K. Kurashige, Y. Toda, S. Matstuishi, K. Hayashi and H. Hosono, *Cryst. Growth Des.*, 2006, **6**, 1602–1605.
36 J. R. Salasin and C. Rawn, *Crystals*, 2017, **7**, 1–25.
37 S. G. Ebbinghaus, H. Krause and F. Syrowatka, *Cryst. Growth Des.*, 2013, **13**, 2990–2994.
38 X. Tao, Y. Yin, Z. Jia, W. Mu, Z. Gao, J. Zhang and X. Tao, *Cryst. Growth Des.*, 2016, **16**, 1903–1906.
39 S. Fujita, H. Nakano, K. Suzuki, T. Mori and H. Masuda, *Catal. Lett.*, 2006, **106**, 139–143.
40 S. Adams and J. Swenson, *Solid State Ionics*, 2004, **175**, 665–669.
41 S. Adams and R. P. Rao, in *Bond Valences*, ed. I. D. Brown and K. R. Poeppelmeier, Springer, Berlin, Heidelberg, 2014, ch. 137, pp. 129–159, DOI: 10.1007/430_2013_137.
42 M. Sale and M. Avdeev, *J. Appl. Crystallogr.*, 2012, **45**, 1054–1056.
43 M. Boyer, X. Yang, A. J. Fernández Carrión, Q. Wang, E. Véron, C. Genevois, L. Hennet, G. Matzen, E. Suard,

D. Thiaudière, C. Castro, D. Pelloquin, L. B. Kong, X. Kuang and M. Allix, *J. Mater. Chem. A*, 2018, **6**, 5276–5289.
44 J. T. S. Irvine and A. R. West, *J. Appl. Electrochem.*, 1989, **19**, 410–412.
45 M. Kilo, S. Swaroop and M. Lerch, *Defect Diffus. Forum*, 2009, **289–292**, 511–516.
46 M. Teusner, R. A. De Souza, H. Krause, S. G. Ebbinghaus, B. Belghoul and M. Martin, *J. Phys. Chem.*, 2015, **119**, 9721–9727.
47 S. Adams and R. P. Rao, *J. Mater. Chem.*, 2012, **22**, 1426–1434.
48 S. Adams, in *Structure and Bonding*, ed. I. D. Brown and K. R. Poeppelmeier, Springer, Berlin, Heidelberg, 2013, vol. 158, ch. 96, pp. 91–128.
49 E. Niwa and M. Yashima, *ACS Appl. Energy Mater.*, 2018, **1**, 4009–4015.
50 Y. Yasui, E. Niwa, M. Matsui, K. Fujii and M. Yashima, *Inorg. Chem.*, 2019, **58**, 9460–9468.
51 L. Pauling, *J. Am. Chem. Soc.*, 1929, **51**, 1010–1026.
52 M. Avdeev, M. Sale, S. Adams and R. P. Rao, *Solid State Ionics*, 2012, **225**, 43–46.
53 I. D. Brown, *Chem. Rev.*, 2009, **109**, 6858–6919.

